

An Information-Theoretic Detector for Multiple Scatterers in SAR Tomography

Pia Addabbo, Senior Member, IEEE, Diego Reale, Member, IEEE, Antonio Pauciullo, Gianfranco Fornaro, Fellow Member, IEEE, and Danilo Orlando, Senior Member, IEEE

Abstract—Persistent scatterer interferometry and Synthetic Aperture Radar (SAR) Tomography are powerful tools for the detection and time monitoring of persistent scatterers. They have been proven to be effective in urban scenarios, especially for buildings and infrastructures 3-D reconstruction and monitoring of deformation. In urban areas, occurrence of layover leads to the presence of multiple contributions within the same image pixel from scatterers located at different heights. In the context of SAR Tomography, this problem can be addressed by considering a multiple hypothesis test to detect the presence of feasible multiple scatterers [1], [2]. In the present paper, we consider this problem in the framework of the information theory and exploit the theoretical tool, developed in [3], to design a one-stage adaptive architecture for multiple hypothesis testing problems in the context of SAR Tomography. Moreover, we resort to the compressive sensing approach for the estimation of the unknown parameters under each hypothesis. This architecture has been verified on both simulated as well as real data also in comparison with suitable counterparts.

Index Terms—Compressing Sensing, Kullback-Leibler Information Criterion, Multiple Alternative Hypotheses, Multiple Scatterers, SAR Tomography, Synthetic Aperture Radar, Sparse Estimation.

I. Introduction

SYNTHETIC Aperture Radar (SAR) Interferometry (InSAR) and, in particular, Differential InSAR (DInSAR) have given an impetus to the use of SAR for monitoring environmental hazards [4], [5], [6]. Modern DInSAR methods, known as Advanced DInSAR (A-DInSAR) techniques, exploit stacks of SAR images acquired on repeated orbits, with time intervals of months or years, to accurately monitor slow ground displacements. Persistent Scatterer Interferometry (PSI) belongs to the class of A-DInSAR techniques. PSI techniques rely on the fact that scatterers with a sufficiently high temporal coherence, i.e., Persistent Scatterers (PS), can be identified at the highest resolution. They are typically located above

This work has been submitted to the IEEE for possible publication. Copyright may be transferred without notice, after which this version may no longer be accessible.

Pia Addabbo is with Università degli Studi “Giustino Fortunato”, viale Raffale Delcogliano, 12, 82100 Benevento, Italy. Email: p.addabbo@unifortunato.eu

Diego Reale, Antonio Pauciullo and Gianfranco Fornaro are with National Research Council - Institute for the Electromagnetic Sensing of the Environment (CNR-IREA), via Diocleziano 328, 80124, Naples, Italy. E-mail: {reale.d, pauciullo.a, fornaro.g}@irea.cnr.it.

Danilo Orlando is with the Department of Information Engineering, University of Pisa, via Girolamo Caruso 16, 56122, Pisa, Italy. Email: danilo.orlando@unipi.it

man-made structures, e.g., buildings or infrastructures, or on exposed rocks. The PSI shows the capabilities of multitemporal/multibaseline interferometry analysis. In fact, the temporal coherence indicator can be exploited as a detector of PSs and allows estimating their position and deformation. Within the framework of multibaseline interferometric stacking, SAR Tomography (TomoSAR) provides a different perspective and processing strategy with respect to PSI. In fact TomoSAR technique, validated both on airborne [7] as well as spaceborne SAR data [8], [9], allows us to frame SAR interferometry into 3D or more multidimensional SAR imaging context. Under this operating approach, PSs appear as scatterers focused along the cross slant range direction. This focusing technique can be extended to the 4D case, which scans the cross slant range-velocity space [10], [11], or even higher dimensions [12], [13].

In this context, the goal is to derive a simple and effective detection scheme that can improve the detection capability of man-made targets in areas with low Signal-to-Noise Ratio (SNR), such as rural areas, at the maximum resolution. The problem of jointly detecting multiple point-like targets is a difficult task since target parameters and, more importantly, the target number are unknown and have to be estimated from the available data. Therefore, unlike conventional detection problems that include two hypotheses, i.e., the noise-only (or null) hypothesis and the signal-plus-noise (or alternative) hypothesis, this lack of a priori information naturally leads to multiple alternative hypotheses (the null hypothesis remains the conventional one). Several strategies have been proposed to address this problem over the years. A detection scheme grounded on Generalized Likelihood Ratio Test (GLRT) for the detection of single scatterers in SAR Tomography was firstly introduced in [14]. Its extension to the multiple hypothesis for the detection of multiple PSs in a tomographic cell test was subsequently proposed in [1]. This detection scheme, based on the cancellation of the first stronger scatterer and therefore referred to as Sequential GLRT with Cancellation (SGLRT-C), implements of a sequence of two decision tests checking for the presence of at maximum one scatterer, thus also limiting the computational requirements. However, the cancellation of the first scatterers limits the super-resolution capability of the detection scheme, i.e. the possibility to detect scatterers below the Rayleigh resolution.

To overcome super-resolution limitations of the SGLRT-

C in [1], a GLRT detector, based on support estimation (Sup-GLRT), for multiple scatterers detection in TomoSAR, has been proposed in [2]. The Sup-GLRT also combines a sequence of two detection stages, with the latter scanning the entire 2-dimensional subspace spanned by the possible two scatterers, thus allowing also achieving super-resolution capabilities. Moreover, in principle, the test could be extended to an arbitrary (> 2) number of interfering scatterers, although this is practically limited by increasing computational efforts. Recently, a solution aimed at reducing the computational cost has been proposed in [15] where a fast Sup-GLRT implementation reducing the computational cost from combinatorial, with respect to all the possible positions in the search grid to linear, at the expense of a reasonable small performance loss, has been preserved. At the design stage, Sup-GLRT exploits a sparsity assumption for the signal model along the elevation (cross slant range) direction, which is often verified in urban areas. Compressed Sensing (CS) is a powerful technique based on the sparsity nature of the signal under investigation [16] and that can be applied to TomoSAR systems [17], [18]. CS reduces the required number of measurements and enhances the elevation resolution [19], [20]. A recent and efficient approach [21] proposes a fast GLRT-based method that bypasses the grid-based search by performing a continuous optimization of an objective function to find suitable estimates of the unknown parameters. To this end, the method uses a quasi-Newton descent algorithm that is initialized and executed under each hypothesis. The experimental results show a superior (detection and estimation) performance with respect to the fast GLRT-based algorithm proposed in [15]. Another interesting approach allowing for super-resolution in TomoSAR is described in [22], where model order selection rules [23] and suitable regularization parameters are incorporated into spectral (or direction) estimation algorithms such as the multiple signal classification and the estimation of signal parameters via rotational invariant techniques. In addition, the authors investigate different methodologies for the proper estimation/selection of the related parameters.

Most of the mentioned solutions are based on a grid of points used to search the most likely values for the unknown parameters. However, as also explained in Section IV, in case of mismatch a performance degradation can occur. To overcome this drawback, gridless solutions were introduced such as in [24], [21, and references therein]. Such solutions are grounded on gradient descent algorithms, atomic norm minimization, particle swarm optimization, and so on. However, both the SGLRT-C and Sup-GLRT experience some issues related to the thresholds setting. Specifically, due to the presence of many alternative hypotheses, a set of thresholds must be considered to select the hypotheses. In fact, existent solutions are based on multiple stages systems which make difficult and time demanding the selection of a suitable threshold to ensure a preassigned Probability of False Alarm (PFA) as well as a reliable probability of correct

classification.

In this paper, we exploit the elegant and systematic framework developed in [3] that is based on the Kullback-Leibler Information Criterion (KLIC) [25]. This design framework considers multiple hypotheses testing problems formed by many alternative hypotheses and only one null hypothesis. Thus, it allows us to suitably handle the lack of information related to the number of PSs. In this context, we design a decision scheme capable of detecting an unknown number of PSs, and estimating their geophysical parameters of interest, i.e. positions and possible displacement rate, in the following referred to as velocity, by using an unique threshold for all the hypotheses. Moreover, we incorporate the CS paradigm within this framework by resorting to a sparse formulation of the related estimation problems. This choice is dictated by the fact that the conventional maximum likelihood approach used in [3] would lead to prohibitive computational requirements. Thus, in the context of the TomoSAR, we merge the CS paradigm and information-theoretic design criterion to come up with a detection architecture, referred to as KLIC-based detector (KLIC-D) that uses a unique threshold to deal with multiple hypotheses unlike existing approaches. It is worth pointing out that the threshold setting for the proposed architecture does not become involved as the number of hypotheses increases. In fact, compared to the Sup-GLRT, the proposed approach offers a significant advantage: the use of a single adaptive threshold (along with a possible design parameter as explained in the next sections) valid for all alternative hypotheses greatly simplifies the design stage while ensuring a constant false alarm rate (CFAR), even when the number of scatterers is unknown. This architecture represents the main technical novelty of this contribution and appears here for the first time (at least to the best of the authors' knowledge). The performance analysis is conducted on both synthetic and real data and a comparison with Sup-GLRT is also carried out. The numerical examples highlight that the proposed architecture returns similar performances to that of the Sup-GLRT without using involved multi-stage decision statistics. As consequence, from a practical point of view, the proposed architecture is more manageable than the considered counterpart especially in the presence of a large number of alternative hypotheses.

The remainder of this paper is organized as follows. In the next section, we provide a formal definition of the signal model and detection problem at hand. In Section III, we derive the adaptive KLIC-D decision scheme and describe the estimation procedures for the unknown parameters. In Section IV, we assess the nominal behavior of the proposed detection algorithm by using synthetic data, whereas in Section V, we present the detection results over real COSMO-SkyMed data. Finally, in Section VI, we draw concluding remarks and trace the route for future research lines.

Notation

In the sequel, vectors and matrices are denoted by boldface lower-case and upper-case letters, respectively. Symbols $(\cdot)^T$, and $(\cdot)^\dagger$ denote transpose and conjugate transpose (Hermitian) operators, respectively. Symbol $\|\cdot\|$ denotes the Euclidean norm of a vector. \mathbb{R} is the set of real numbers, and $\mathbb{R}^{N \times M}$ is the Euclidean space of $(N \times M)$ -dimensional real matrices (or vectors if $M = 1$). \mathbb{C} is the set of complex numbers, and $\mathbb{C}^{N \times M}$ is the Euclidean space of $(N \times M)$ -dimensional complex matrices (or vectors if $M = 1$). If \mathbf{a} is an N -dimensional vector, then $\text{diag}(\mathbf{a})$ is an $N \times N$ diagonal matrix whose nonzero entries are the elements of \mathbf{a} . Symbol \mathbf{I} stands for the identity matrix of proper size. Given a generic hypothesis denoted by H , \bar{H} is the complement of H . The acronym PDF stands for Probability Density Function and the conditional PDF of a random variable x given another random variable y is denoted by $f(x|y)$. Finally, we write $\mathbf{x} \sim \mathcal{CN}_N(\boldsymbol{\mu}, \mathbf{M})$ if \mathbf{x} is a complex circular N -dimensional normal vector with mean $\boldsymbol{\mu}$ and positive definite covariance matrix \mathbf{M} .

II. Signal model and Problem Formulation

Let us consider N SAR images acquired at different time epochs $t_n, n = 1, \dots, N$. The received signal in any image pixel, after coregistration with respect to a given (reference) image and atmospheric effects compensation, can be modeled as the superposition of elementary contributions distributed along the elevation direction s , also referred to as slant-height, orthogonal to radar line-of-sight r , and related to the height $z = s \sin(\theta)$, with θ being the incidence angle, see Figure 1, [10]:

$$x_n = \int_{\Delta s} \gamma(s) e^{-j\frac{4\pi}{\lambda}d(s,t_n)} e^{-j2\pi\xi_n s} ds, \quad (1)$$

where:

- $\gamma(s) \in \mathbb{C}$ is the distribution of the backscattering coefficient along s . We assume $\gamma(s)$ to be constant over the time;
- $d(s, t_n) \in \mathbb{R}$ is the distance variation at the different acquisition epochs;
- $\xi_n = \frac{2b_n}{\lambda r_0}$ represents the spatial frequency with b_n being perpendicular baseline of the n -th acquisition, r_0 the distance of the target from the reference track, and λ the system wavelength;
- Δs is the extent of the scene in elevation direction.

The exponential deformation term in (1) can be expanded as the 2D-Fourier transform of a suitable function $g(s, v, l)$ [12], i.e.,

$$e^{-j\frac{4\pi}{\lambda}d(s,t_n)} = \int_{\Delta v} \int_{\Delta l} g(s, v, l) e^{-j2\pi(\eta_n v + \zeta_n l)} dv dl, \quad (2)$$

where v and l , associated with the Fourier mate variables $\eta_n = \frac{2t_n}{\lambda}$ and $\zeta_n = \frac{2T_n}{\lambda}$, with T_n being the temperatures at the acquisition epochs, play the role of velocity and of thermal dilation coefficients. Substituting (2) in (1), we have

$$x_n = \int_{\Delta s} \int_{\Delta v} \int_{\Delta l} \gamma(s, v, l) e^{-j2\pi(\xi_n s + \eta_n v + \zeta_n l)} ds dv dl, \quad (3)$$

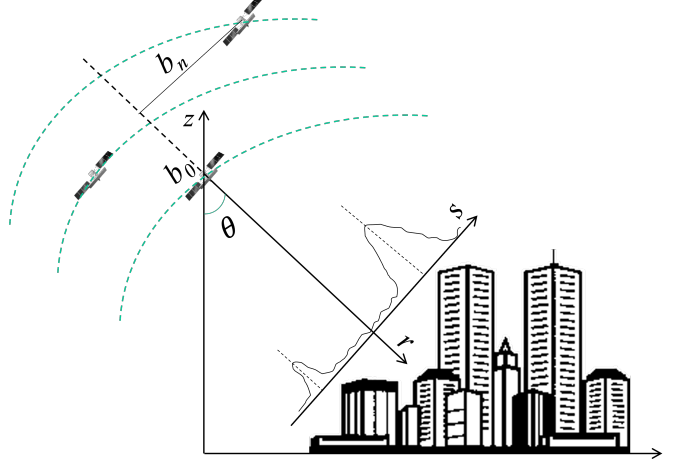


Fig. 1. Multi-temporal tomographic SAR geometry, with the radar acquiring from different positions separated by $b_n, n = 1, \dots, N$; θ is the look angle, s is the elevation direction (orthogonal to the line-of-sight r).

with $\gamma(s, v, l) = \gamma(s)g(s, v, l)$.

Let us rearrange the received signal in vector form and consider $\mathbf{x} \in \mathbb{C}^{N \times 1}$, the vector collecting, for each pixel, the measured complex data from the N images. Assuming concentrated scattering in (3) and considering the noise component, the signal vector can be expressed as the superposition of an unknown number, say $K \leq K_{\max}$, of fully coherent scatterers [26]:

$$\mathbf{x} = \sum_{k=1}^K g_k \mathbf{a}(\mathbf{p}_k) + \mathbf{w}, \quad (4)$$

where:

- $\mathbf{w} \sim \mathcal{CN}_N(\mathbf{0}, \sigma^2 \mathbf{I})$ is the disturbance vector with $\sigma^2 > 0$;
- $g_k \in \mathbb{C}, k = 1, \dots, K$, is the unknown k th complex backscattering coefficient;
- $\mathbf{p}_k = [s_k, v_k, l_k]^T \in \mathbb{R}^{3 \times 1}, k = 1, \dots, K$, represents the unknown k th scatterer position in the parameter space;
- $\mathbf{a}(\mathbf{p}_k) \in \mathbb{C}^{N \times 1}, k = 1, \dots, K$, is the normalized steering vector (i.e., $\|\mathbf{a}(\mathbf{p}_k)\| = 1$). The n th component of the k th steering vector is given by $\{\mathbf{a}(\mathbf{p}_k)\}_n = \frac{1}{\sqrt{N}} \exp(-j2\pi \zeta_n^T \mathbf{p}_k)$, with $\zeta_n = [\xi_n, \eta_n, \zeta_n]^T$ being the vector collecting the frequencies associated with the parameters in \mathbf{p}_k .

Defining the steering matrix $\mathbf{A}_K = [\mathbf{a}(\mathbf{p}_1), \dots, \mathbf{a}(\mathbf{p}_K)] \in \mathbb{C}^{N \times K}$, we can rewrite the observation vector according to the following linear model

$$\mathbf{x} = \mathbf{A}_K \mathbf{g}_K + \mathbf{w}, \quad (5)$$

where $\mathbf{g}_K = [g_1, \dots, g_K]^T$ is the backscattering coefficients' vector.

Now, the problem of detecting, pixel by pixel, an unknown number, say $k \in \{1, \dots, K_{\max}\}$, of scatterers,

whose related parameters, say \mathbf{p}_k , are unknown, can be formulated as the following multiple hypothesis test

$$\begin{cases} H_0 & : \mathbf{x} = \mathbf{w}, \\ H_1 & : \mathbf{x} = \mathbf{A}_1 \mathbf{g}_1 + \mathbf{w}, \\ & \vdots \\ H_k & : \mathbf{x} = \mathbf{A}_k \mathbf{g}_k + \mathbf{w}, \\ & \vdots \\ H_{K_{\max}} & : \mathbf{x} = \mathbf{A}_{K_{\max}} \mathbf{g}_{K_{\max}} + \mathbf{w}. \end{cases} \quad (6)$$

Finally, for the subsequent developments, it is worth providing the PDF of \mathbf{x} , under H_0 , that is

$$f_0(\mathbf{x}; \sigma^2) = \frac{1}{\pi^N (\sigma^2)^N} \exp \left\{ -\frac{\|\mathbf{x}\|^2}{\sigma^2} \right\}, \quad (7)$$

and that under the generic H_k hypothesis, $k = 1, \dots, K_{\max}$, namely

$$f_{1,k}(\mathbf{x}; \sigma^2, \mathbf{A}_k, \mathbf{g}_k) = \frac{1}{\pi^N (\sigma^2)^N} \exp \left\{ -\frac{\|\mathbf{x} - \mathbf{A}_k \mathbf{g}_k\|^2}{\sigma^2} \right\}. \quad (8)$$

III. Multiple scatterers Detection

In this section, we devise a detection architecture for problem (6) that is based upon the Penalized Log-Likelihood Ratio Test (PLLRT) [3], [27]. Actually, we heuristically modify the PLLRT by replacing the maximum likelihood estimates of the unknown parameters under the multiple alternative hypotheses (e.g., $\mathbf{p}_1, \dots, \mathbf{p}_k$, and \mathbf{g}_k in addition to k) with suitable estimates obtained by means of the iterative procedure described below. This choice is dictated by the fact that the maximum likelihood approach leads to intractable mathematics and/or time demanding optimization approaches. Therefore, we start from the general form for the PLLRT given by

$$\max_{k \in \{1, 2, \dots, K_{\max}\}} \left\{ \max_{\sigma^2, \mathbf{A}_k, \mathbf{g}_k} \log[f_{1,k}(\mathbf{x}; \sigma^2, \mathbf{A}_k, \mathbf{g}_k)] - \max_{\sigma^2} \log[f_0(\mathbf{x}; \sigma^2)] - h(k) \right\} \begin{matrix} \geq \\ \leq \end{matrix}_{H_0}^{\hat{H}_k} \eta, \quad (9)$$

where \hat{k} maximizes the left-hand side of the above equation, η is the detection threshold set according to a given PFA, defined as $P_{fa} = P(\text{accept } \hat{H}_k | H_0)$, $h(k)$ is a penalty term depending on the number of unknown parameters of interest [28] and, inspired by the generalized information criterion, under the k -th alternative hypothesis, it is given by

$$h(k) = \frac{6k}{2} (1 + \rho) \quad (10)$$

with $\rho > 1$ a constant design parameter. This parameter is inherited from the generalized information criterion [3], [23]. It represents a degree of freedom that allows for a control of the probability of overestimating the number of scatterers. Actually, it depends on the performance metrics, the number of samples, and the data-generating

mechanism itself; more importantly, there does not exist a clear indication of how ρ can be selected [23, and references therein]. For this reason, in what follows, this parameter is set by heuristically evaluating the probability of misclassification (see Section IV for further details).

Solving the joint maximization problem with respect to the unknown parameters is involved from a mathematical point of view (at least to the best of the authors' knowledge). For this reason, we exploit the following two-step procedure. First, we assume that σ^2 is known and estimate \mathbf{A}_k , $k = 1, \dots, K_{\max}$, by means of a compressive sensing strategy as described in Subsection III-A. Then, we use these estimates to compute the logarithm of the GLRT under each hypothesis. Recall that the overall (suboptimum) GLRT is derived under the assumption that σ^2 and \mathbf{g}_k , $k = 1, \dots, K_{\max}$, are unknown.

In fact, once the estimates of the \mathbf{A}_k s, say $\hat{\mathbf{A}}_k$, are available, we consider the following optimization problems. Under H_1 , we obtain

$$\begin{aligned} & \max_{\mathbf{g}_k} \max_{\sigma^2} \left[-N \log(\pi) - N \log(\sigma^2) - \frac{1}{\sigma^2} \|\mathbf{x} - \hat{\mathbf{A}}_k \mathbf{g}_k\|^2 \right] \\ &= \max_{\mathbf{g}_k} \left[C - N \log(\|\mathbf{x} - \hat{\mathbf{A}}_k \mathbf{g}_k\|^2) \right] \\ &= C - N \log(\mathbf{x}^\dagger \mathbf{P}_{\hat{\mathbf{A}}_k}^\perp \mathbf{x}), \end{aligned} \quad (11)$$

where $C = -N \log(\pi) - N + N \log N$ and $\mathbf{P}_{\hat{\mathbf{A}}_k}^\perp = \mathbf{I} - \hat{\mathbf{A}}_k (\hat{\mathbf{A}}_k^\dagger \hat{\mathbf{A}}_k)^{-1} \hat{\mathbf{A}}_k^\dagger$ is the projection matrix onto the orthogonal complement of the subspace spanned by the columns of $\hat{\mathbf{A}}_k$. Notice that the maximum likelihood estimate of σ^2 assuming that $\mathbf{A}_k = \hat{\mathbf{A}}_k$ is given by

$$\hat{\sigma}_k^2 = \frac{1}{N} \|\mathbf{x} - \hat{\mathbf{A}}_k \hat{\mathbf{g}}_k\|^2 = \frac{1}{N} \|\mathbf{P}_{\hat{\mathbf{A}}_k}^\perp \mathbf{x}\|^2, \quad (12)$$

where $\hat{\mathbf{g}}_k = (\hat{\mathbf{A}}_k^\dagger \hat{\mathbf{A}}_k)^{-1} \hat{\mathbf{A}}_k^\dagger \mathbf{x}$. Under H_0 , the problem at hand is

$$\begin{aligned} & \max_{\sigma^2} \left[-N \log(\pi) - N \log(\sigma^2) - \frac{1}{\sigma^2} \|\mathbf{x}\|^2 \right] \\ &= C - N \log(\mathbf{x}^\dagger \mathbf{x}). \end{aligned} \quad (13)$$

Gathering the above results, the final expression for the detector (up to irrelevant constants) is

$$\max_{k \in \{1, 2, \dots, K_{\max}\}} \left\{ N \log \left[\frac{\mathbf{x}^\dagger \mathbf{x}}{\mathbf{x}^\dagger \mathbf{P}_{\hat{\mathbf{A}}_k}^\perp \mathbf{x}} \right] - \frac{6k}{2} (1 + \rho) \right\} \begin{matrix} \geq \\ \leq \end{matrix}_{H_0}^{\hat{H}_k} \eta \quad (14)$$

and it will be referred to in the following as KLIC-based Detector (KLIC-D).

A. Estimation procedure of the \mathbf{A}_k s based on compressive sensing

To effectively apply the compressive sensing paradigm, it is necessary to bring to light the sparse nature of the signal model. To this end, we consider an augmented steering matrix, say \mathbf{A} , which includes all the possible values assumed by \mathbf{p}_k and a corresponding vector \mathbf{g} , where the nonzero entries are those associated with the \mathbf{p}_k s that

are true. As a consequence, \mathbf{g} is sparse, \mathbf{A} represents the dictionary of the compressed sensing algorithm, and the signal model becomes

$$\mathbf{x} = \mathbf{Ag} + \mathbf{w}, \quad (15)$$

where $\mathbf{A} = [\mathbf{a}(\mathbf{p}_1), \dots, \mathbf{a}(\mathbf{p}_{K_p})] \in \mathbb{C}^{N \times K_p}$ and $\mathbf{g} \in \mathbb{C}^{K_p \times 1}$, with $K_p \gg K_{\max}$ to account for K_{\max} alternative hypotheses and to guarantee sparsity.

At the design stage, we assume that \mathbf{g} obeys a sparsity-promoting prior. Actually, in literature, several sparsity-promoting priors can be found that exhibit different properties. However, in what follows, we adopt a Laplace-based improper prior (i.e., it is not guaranteed that its integral is finite) [29], [30] since it allows for mathematical tractability (in fact, we come up with a closed-form expression for the estimate of the prior parameter) and, even though it does not share any known optimality property, reliable estimation results can be obtained from the application of this prior (or suitable modifications of it). Specifically, its expression is given by

$$g(\mathbf{g}; \alpha) = \frac{\alpha^{K_p}}{(2\pi)^{K_p}} \exp\left\{-\sqrt{\alpha}\left(\sum_{k=1}^{K_p} |g_k| + 1\right)\right\} \quad (16)$$

with $\alpha > 0$ a parameter that controls sparsity. Thus, the optimization problem can be written as

$$\max_{\mathbf{g}, \alpha} \log [f_{1, K_p}(\mathbf{x}, \mathbf{g}; \sigma^2, \alpha)]. \quad (17)$$

Now, notice that under H_k , the joint PDF of \mathbf{x} and \mathbf{g} can be written as

$$\begin{aligned} & f_{1, K_p}(\mathbf{x}, \mathbf{g}; \sigma^2, \alpha) \quad (18) \\ &= f_{1, K_p}(\mathbf{x} | \mathbf{g}; \sigma^2)g(\mathbf{g}; \alpha) \\ &= \frac{1}{(\pi)^N (\sigma^2)^N} \exp\left\{-\frac{1}{\sigma^2} \|\mathbf{x} - \mathbf{Ag}\|^2\right\} \\ &\quad \times \frac{\alpha^{K_p}}{(2\pi)^{K_p}} \exp\left\{-\sqrt{\alpha}\left(\sum_{k=1}^{K_p} |g_k| + 1\right)\right\}. \end{aligned}$$

Then, taking the logarithm, the optimization problem can be recast as

$$\begin{aligned} & \max_{\alpha} \max_{\mathbf{g}} \left[-N \log(\pi) - N \log(\sigma^2) - \frac{1}{\sigma^2} \|\mathbf{x} - \mathbf{Ag}\|^2 \right. \\ & \quad \left. + K_p \log(\alpha) - K_p \log(2\pi) - \sqrt{\alpha} \left(\sum_{k=1}^{K_p} |g_k| + 1 \right) \right]. \quad (19) \end{aligned}$$

Let us start from the optimization with respect to α and notice that

$$\lim_{\alpha \rightarrow 0} \log(f_{1, K_p}) = -\infty \quad (20)$$

and

$$\lim_{\alpha \rightarrow +\infty} \log(f_{1, K_p}) = -\infty. \quad (21)$$

Thus, setting to zero the first derivative of the objective function with respect to α , we obtain the following equality

$$\frac{K_p}{\alpha} - \frac{1}{2\sqrt{\alpha}} \left(\sum_{k=1}^{K_p} |g_k| + 1 \right) = 0, \quad (22)$$

and, hence,

$$\hat{\alpha} = \frac{4K_p^2}{\left(\sum_{k=1}^{K_p} |g_k| + 1 \right)^2}. \quad (23)$$

Replacing (23) in (19), we come up with

$$\begin{aligned} & \max_{\mathbf{g}} \left[-N \log(\pi) - N \log(\sigma^2) - \frac{1}{\sigma^2} \|\mathbf{x} - \mathbf{Ag}\|^2 \right. \\ & \quad \left. + 2K_p \log\left(\frac{2K_p}{\sum_{k=1}^{K_p} |g_k| + 1}\right) - K_p \log(2\pi) - 2K_p \right] \\ &= \max_{\mathbf{g}} \left[-N \log(\pi) - N \log(\sigma^2) - \frac{1}{\sigma^2} \|\mathbf{x} - \mathbf{Ag}\|^2 \right. \\ & \quad \left. + 2K_p \log(2K_p) - 2K_p \log\left(\sum_{k=1}^{K_p} |g_k| + 1\right) \right. \\ & \quad \left. - K_p \log(2\pi) - 2K_p \right]. \quad (24) \end{aligned}$$

It is not difficult to show that when $\|\mathbf{g}\| \rightarrow +\infty$, the last objective function tends to $-\infty$. Thus, setting its derivative with respect to \mathbf{g} to zero leads to

$$-\frac{1}{\sigma^2} \left(\mathbf{A}^\dagger \mathbf{Ag} - \mathbf{A}^\dagger \mathbf{x} \right) - K_p \frac{1}{\sum_{k=1}^{K_p} |g_k| + 1} \mathbf{B} \mathbf{g} = \mathbf{0} \quad (25)$$

with

$$\mathbf{B} = \text{diag}\left(\frac{1}{|g_1|}, \dots, \frac{1}{|g_{K_p}|}\right), \quad (26)$$

and the final result is

$$\mathbf{g} = \left[\frac{1}{\sigma^2} \mathbf{A}^\dagger \mathbf{A} + \frac{K_p}{\sum_{k=1}^{K_p} |g_k| + 1} \mathbf{B} \right]^{-1} \frac{1}{\sigma^2} \mathbf{A}^\dagger \mathbf{x}. \quad (27)$$

We proceed by iterating (27) as follows

$$\begin{aligned} \hat{\mathbf{g}}^{(t+1)} &= \left[\frac{1}{\sigma^2} \mathbf{A}^\dagger \mathbf{A} + \frac{K_p}{\sum_{k=1}^{K_p} |g_k^{(t)}| + 1} \mathbf{B}^{(t)} \right]^{-1} \frac{1}{\sigma^2} \mathbf{A}^\dagger \mathbf{x} \quad (28) \\ &= \mathbf{C}^{(t)} \mathbf{A}^\dagger [\sigma^2 \mathbf{I} + \mathbf{A} \mathbf{C} \mathbf{A}^\dagger]^{-1} \mathbf{x}, \quad (29) \end{aligned}$$

where the last equality derives from the Woodbury identity [31] and

$$\mathbf{C}^{(t)} = \frac{\sum_{k=1}^{K_p} |g_k^{(t)}| + 1}{K_p} \text{diag}(|g_1^{(t)}|, \dots, |g_{K_p}^{(t)}|). \quad (30)$$

Following the lead of [28], it is possible to show that the iteration procedure gives rise to a nondecreasing sequence of the objective function. We stop iterating when t reaches a chosen value \bar{t} or when a suitable stopping criterion is satisfied as indicated in Algorithm 1 where a schematic summary of the procedure is reported, including the initialization of the \hat{g}_k s. In this respect, we consider a matched-filter-based initialization strategy that projects data vector onto each column of the dictionary. This kind

Algorithm 1 Compressive sensing algorithm to estimate the \mathbf{A}_k s

Input: $\bar{t}, \Delta, \sigma^2, \mathbf{x}, \mathbf{A}$

Output: $\widehat{\mathbf{A}}_k, k = 1, \dots, K_{\max}$

1: Set $t = 0$, $\widehat{g}_k^{(0)} = |\mathbf{a}^\dagger(\mathbf{p}_k)\mathbf{x}|$, $k = 1, \dots, K_P$,

2: Set $t = t + 1$

3: Compute

$$\mathbf{C}^{(t-1)} = \frac{\sum_{k=1}^{K_p} |g_k^{(t-1)}| + 1}{K_p} \text{diag}(|g_1^{(t-1)}|, \dots, |g_{K_p}^{(t-1)}|)$$

4: Compute

$$\widehat{\mathbf{g}}^{(t)} = \mathbf{C}^{(t-1)} \mathbf{A}^\dagger [\sigma^2 \mathbf{I} + \mathbf{A} \mathbf{C} \mathbf{A}^\dagger]^{-1} \mathbf{x}$$

5: If $\bar{t} = t + 1$ or $\frac{\|\widehat{\mathbf{g}}^{(t)} - \widehat{\mathbf{g}}^{(t-1)}\|}{\|\widehat{\mathbf{g}}^{(t)}\|} < \epsilon$ go to step 6 else go to step 2

6: Select the k highest peaks of $\widehat{\mathbf{g}}^{(\bar{t})}$ and form $\widehat{\mathbf{A}}_k = [\mathbf{a}(\mathbf{p}_1), \dots, \mathbf{a}(\mathbf{p}_k)]$ for all $k = 1, \dots, K_{\max}$

7: Return $\widehat{\mathbf{A}}_k, k = 1, \dots, K_{\max}$

of initialization exploits the properties of the matched filter and the inherent correlation between the measurements and the dictionary. It is clear that other strategies are possible, such as a random selection of the initial point, but, as shown in the next sections, this matched-filter-based strategy allows for a stable convergence of the iterative algorithm and leads to reliable performance. Therein, the parameter $\epsilon > 0$ allows for a control of the number of iterations. The required value for \bar{t} is determined by analyzing the convergence rate. After \bar{t} iterations, we select the $k < N$ highest peaks of $\widehat{\mathbf{g}}^{(\bar{t})}$ to form $\widehat{\mathbf{A}}_k, k = 1, \dots, K_{\max}$, for all alternative hypotheses in (6). It is worth of noting that the maximum number \bar{t} of iterations is independent of the maximum number K_{\max} of scatterers to be detected. Finally, we compute the PLLRT substituting the parameters with the respective estimates as depicted in Figure 2. From inspection of Algorithm 1, the computational cost of the sparse estimation procedure in terms of the usual Landau notation is $\mathcal{O}(K_{\max}(N^3 + N^2 + 3K_P N + 2N)) \approx \mathcal{O}(K_{\max}N^3)$, where K_{\max} depends on the specific application.

IV. Performance Analysis on Synthetic Data

In this section, we assess the nominal behavior of the proposed detector on simulated data in terms of false alarm rate, detection probabilities, and estimation error. Moreover, we compare these results with those returned by the most natural counterpart, i.e., the Sup-GLRT method [2].

In the numerical examples, we simulated data according to the acquisition parameters of a real X-band data set, composed by $N = 38$ SAR images. Particularly, the system parameters are related to the real COSMO-SkyMed dataset exploited in the next section, where the

experiments are carried out on real data. The distribution of the acquisitions, in the temporal/perpendicular baseline domain, is reported in Figure 3. The spans of the perpendicular and temporal baselines are $\Delta B \sim 2100$ m and $\Delta t = 971$ days (~ 2.65 years), corresponding to nominal Rayleigh resolutions [10] in elevation $\delta_s = \lambda r_0 / (2\Delta B) \approx 5.45$ m (related to the height resolution $\delta z \approx 3.08$ m, being $\theta = 34.4^\circ$) and velocity $\delta v = \lambda / (2\Delta t) \approx 0.59$ cm/year, being $\lambda = 3.1$ cm and $r_0 = 745$ km.

As for the position of the scatterer in the parameter space, $\mathbf{p}_k, k = 1, \dots, K_p$, the values of the elevation s vary in $[-177, 177]$ m ($[-100, 100]$ m in terms of height), while those of the velocity v take on values in $[-1, 1]$ cm/year. Elevation and velocity intervals are sampled with a spacing equal to half of the corresponding nominal resolution. Notice that when the actual position of the point scatterer is not exactly aligned with the grid points, a performance degradation can occur that depends on the extent of the deviation between the actual steering vector and the nominal steering vectors belonging to the search grid. In order to mitigate this loss, an effective strategy could consist in repeating the entire estimation procedure with the same number of grid points but the parameter range of variation restricted around the estimates returned at the previous iteration. Doing so, the computational load of each iteration would remain unaltered (namely that of the sparse estimation procedure) while the overall computational cost becomes proportional to the number of iterations (as shown below the computational complexity depends on the size of the search grid and, hence, increasing the cardinality of the grid could lead to prohibitive execution times). As an alternative, interpolation strategies can be pursued to reduce this straddle loss. For the comparison analysis between Sup-GLRT and the KLIC-D, we assume that the maximum number of scatterers within a tomographic cell is equal to $K_{\max} = 2$. Subsequently, we extend the performance analysis of KLIC-D to the case of $K_{\max} = 3$.

In what follows, the figures of merit are:

- the Probability of Detection under H_i , say $P_{d,H_i} = P(\text{accept } \bar{H}_0 | H_i)$ as a function of the SNR = g^2 / σ^2 , with $g > 0$ the modulus of the reference PS backscattering coefficient and $\sigma^2 = 1$;
- the Root Mean Square Error (RMSE) for the estimate of the number of scatterers as a function of the SNR under H_i , defined as

$$R_{K,H_i} = \sqrt{\left(\sum_{l=1}^{N_{MC}} \left| K - \widehat{K}_i(l) \right|^2 \right) / N_{MC}}$$

where $\widehat{K}_i(l)$ is the estimate of the number of scatterers at the l th Monte Carlo (MC) trial under H_i , while N_{MC} represents the total number of MC trials;

- the probability of correct classification, say $P_{c,H_i} = P(H_i | H_i)$, $i = 1, \dots, K_{\max}$;

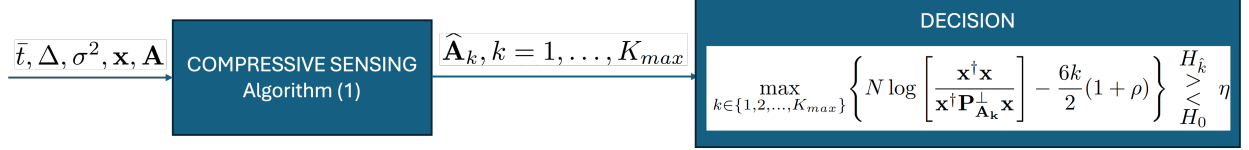


Fig. 2. Block scheme for the proposed multiple hypothesis test.

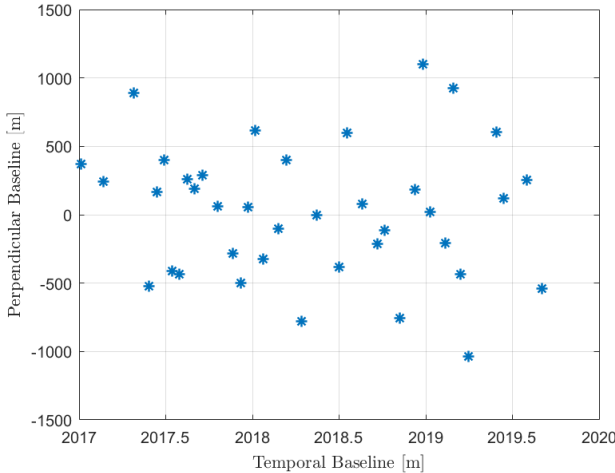


Fig. 3. Distribution of the acquisitions, reported as stars, in the Temporal / Spatial Baseline domain.

- the RMSE of the estimated scatterer localization in terms of height and velocity:

$$R_{h,H_i} = \sqrt{\left(\sum_{l=1}^{N_{MC}} |z - \hat{z}_i(l)|^2 \right) / N_{MC}},$$

where $\hat{z}_i(l)$ is the estimate of scatterer height [m] at the l th MC under H_i , $i = 1, \dots, K_{\max}$, and,

$$R_{v,H_i} = \sqrt{\left(\sum_{l=1}^{N_{MC}} |v - \hat{v}_i(l)|^2 \right) / N_{MC}},$$

where $\hat{v}_i(l)$ is the estimate of scatterer velocity [cm/year] at the l th MC under H_i , $i = 1, \dots, K_{\max}$.

The above estimates are obtained over 5000 independent MC trials, while the detection thresholds are computed via $100/P_{fa}$ runs, with $P_{fa} = 10^{-3}$. The value of the parameter ρ , in (10), is set to 3, since this choice ensures a probability of selecting hypothesis H_2 under H_1 , i.e., $P(\text{accept } H_2 | H_1)$, equal to 10^{-3} for $K_{\max} = 2$ and SNR = 15 dB. For $K_{\max} = 3$, the parameter ρ is set to 5 in order to guarantee the same misclassification probability.

1) Convergence analysis and False Alarm probability: As a preliminary step, we analyze the necessary number of iterations \bar{t} required for the compressive sensing algorithm and its convergence rate. To this end, in Figure 4, we plot the values of the relative variation of the compressed log-likelihood, i.e.,

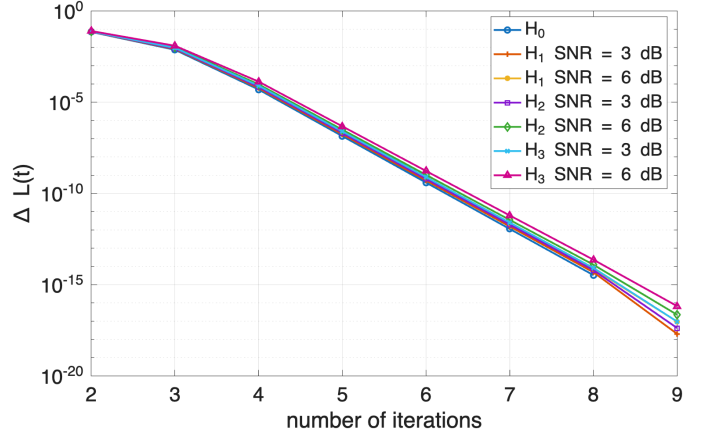


Fig. 4. Relative variation of the log-likelihood (19) versus the number of iterations for the compressive sensing algorithm.

$$\Delta L(t) = \left| \left(L(t) - L(t-1) \right) / L(t) \right| \quad (31)$$

where

$$L(t) = \log \left[f_{1,K_P}(\mathbf{x}, \hat{\mathbf{g}}^{(t)}; \sigma^2, \hat{\alpha}) \right], \quad (32)$$

with $\sigma^2 = 1$, averaged over 1000 MC versus t , under H_0 , H_1 , H_2 , and H_3 with SNR = 3, 6 dB. It turns out that, for the chosen parameters, 6 iterations are sufficient to achieve a variation lower than 10^{-8} for all the situations considered. Thus, in what follows, we set $\bar{t} = 6$.

Moreover, we evaluate the robustness of the PFA in the presence of a mismatch between the assumed and actual noise variance. Particularly, Figure 5 presents a sensitivity analysis of P_{fa} as a function of the noise variance parameter which ranges from 1 to 1000, whereas the threshold is estimated by assuming $\sigma^2 = 1$. The analysis reveals that as the noise variance increases well beyond the value used to estimate the nominal detection threshold, the PFA remains constant, at least for the considered simulation setup. For this reason, in the following and in the real data analysis, we set $\sigma^2 = 1$.

2) Comparison with the Sup-GLRT: Here, we compare the performance of the KLIC-D with the Sup-GLRT proposed in [2]. For the ease of the reader, we provide the expression of the Sup-GLRT: the decision at the k th

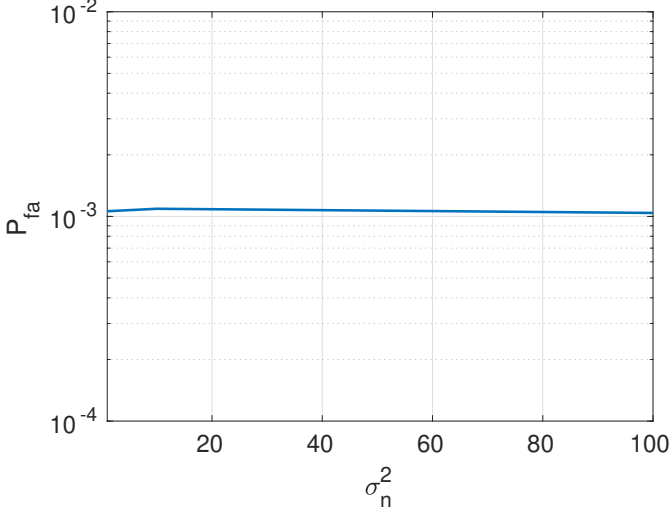


Fig. 5. Sensitivity analysis of P_{fa} a with respect to mismatched σ parameter (threshold is estimated with $\sigma^2 = 1$).

stage, with $k = 1, \dots, K_{\max}$, compares the statistic to a threshold to select either H_{k-1} or $H_{K_{\max}}$, that is

$$\Lambda_k(\mathbf{x}) = \frac{\min_{\mathbf{A}_{k-1}} \mathbf{x}^\dagger \mathbf{P}_{\mathbf{A}_{k-1}}^\perp \mathbf{x}}{\min_{\mathbf{A}_{K_{\max}}} \mathbf{x}^\dagger \mathbf{P}_{\mathbf{A}_{K_{\max}}}^\perp \mathbf{x}} \begin{cases} > & H_{K \geq k} \\ < & \eta_k, \end{cases} \quad (33)$$

where η_k , $k = 1, \dots, K_{\max}$, are the detection thresholds. It should be noted that (33) requires a sequential multistage detection process, where each stage requires a thresholds. On the other hand, KLIC-D exploits a single adaptive threshold for all hypotheses (in addition to a tuning parameter). This significantly simplifies threshold setting. To limit the computational burden of Sup-GLRT, in the following analysis, we set $K_{\max} = 2$.

Figures 6 and 7 show the results of the comparison. In particular, Figure 6 show the results in terms of P_{d,H_i} , $i = 1, 2$, as functions of the SNR that takes on values in the interval [0, 25] dB, when H_i , $i = 1, 2$ are in force (the true hypothesis is indicated in the figure's legend). We consider two different configurations for the proposed detector: $K_{\max} = 2$ and $K_{\max} = 3$ (please notice that it is not easy to consider the latter case for Sup-GLRT from the computational point of view, as the implementation of the projector into the subspace spanned by all possible combinations of the three scatterers is required in (33)). The analysis is carried out considering different configurations in terms of scatterer position and power. In the first case of Figure 6 (top), the scatterers have the same power levels and fixed positions (the first target is located in the center of the steering matrix, while the second target is placed at an elevation distance of 30.8 m and with the same velocity). The detection probability under H_2 is higher than under H_1 , since multiple scatterers contribute to increase the backscattered power within the same tomographic cell. The detectors share a similar detection performance under both hypotheses. In the second case

(middle subfigure), the scatterers are randomly positioned within the nominal resolution cells. Performance slightly degrades compared to the fixed-position scenario due to the spatial variability. In the third case (bottom), the scatterers exhibit different power levels:¹

- under H_1 , the backscattering coefficients are set as $|g_1|^2 = g^2$;
- under H_2 , they are defined as $|g_1|^2 = g^2$ and $|g_2|^2 = 1.5g^2$, leading to an increased power imbalance.

As expected, the detection probability when H_2 is in force is better than under H_1 since the additional scatterer has higher power. The detection probability benefits from the presence of multiple scatterers, especially at higher SNR values.

Figure 7 illustrates R_{K,H_i} as a function of SNR. As expected, at low SNR, the estimation error is relatively high because weaker scatterers are harder to distinguish from noise. As SNR increases, the RMSE significantly decreases, indicating a more accurate estimation of the number of scatterers. When scatterers have different power levels (bottom subfigure), the RMSE is slightly higher than in the equal-power cases. This is expected, as the imbalance in backscattering power can lead to a wrong estimation of the scatterer number, particularly for high SNR.

Figure 8 illustrates the probability of correct classification versus SNR for the proposed KLIC-D and the Sup-GLRT under different scatterer configurations. As expected, at low SNR, this probability is relatively low, but, as the SNR increases, it significantly increases under both hypotheses, indicating a more accurate estimation of the number of scatterers. In scenarios with equal scattering coefficients and fixed positions (top subfigure), KLIC-D achieves performance comparable to the competitor, successfully leveraging the increased backscattered power from multiple scatterers to enhance P_{c,H_2} . While KLIC-D remains computationally feasible and structurally scalable to $K_{\max} = 3$, the probability of correct classification is lower than that in scenarios with $K_{\max} = 2$. This would be a natural behavior as the increased number of alternative hypotheses introduces additional uncertainty in distinguishing the exact number of scatterers, particularly at low to moderate SNR levels. The introduction of random scatterer positions leads to a modest performance degradation due to spatial variability, yet the detector maintains reliable performance. In the cases with unbalanced scattering coefficients, KLIC-D obtains better performance, particularly at moderate to high SNR levels.

Figures 9-12 show the RMSE for estimating the height and velocity under H_1 and H_2 . The monotonic decrease in RMSE with increasing SNR for both methods confirms the expected estimation behavior. Notably, the proposed KLIC-D exhibits localization accuracy that is almost identical to or better than the Sup-GLRT across the entire SNR range. This result validates that the integration

¹For simplicity, we assume that the phases of the g_k s are equal to zero.

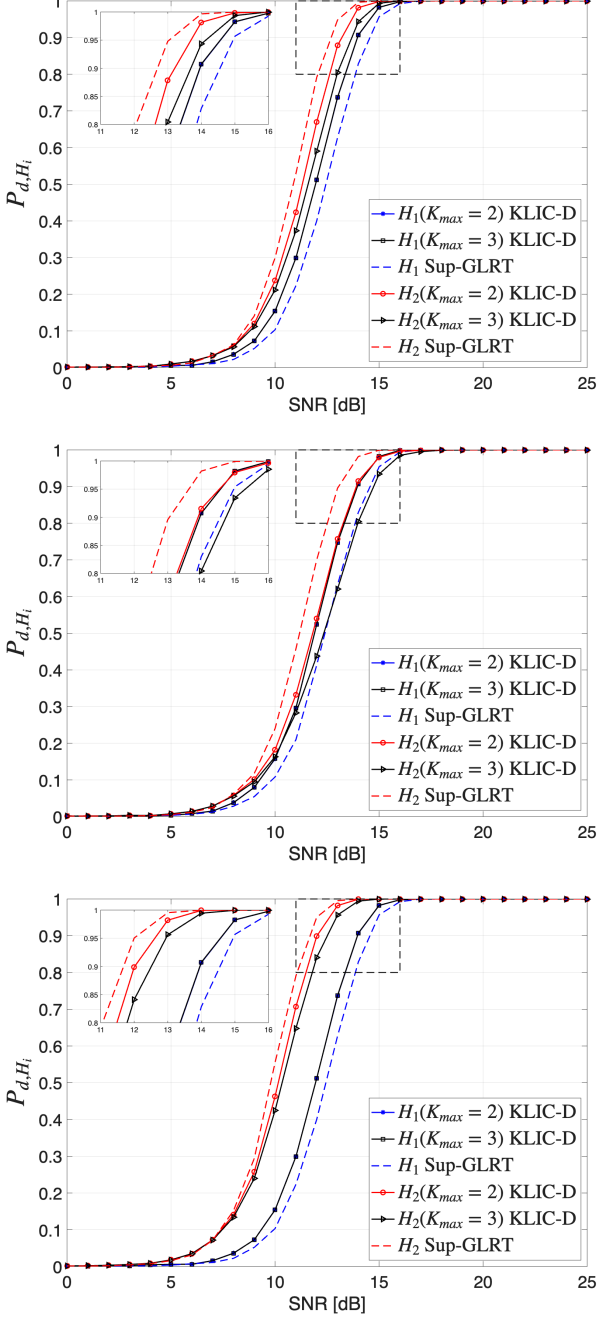


Fig. 6. Probability of Detection P_{d,H_i} , $i = 1, 2$ versus SNR [dB], assuming the same scattering coefficients and fixed positions (at the top) and random positions (at the middle), assuming different scattering coefficients and fixed positions (at the bottom).

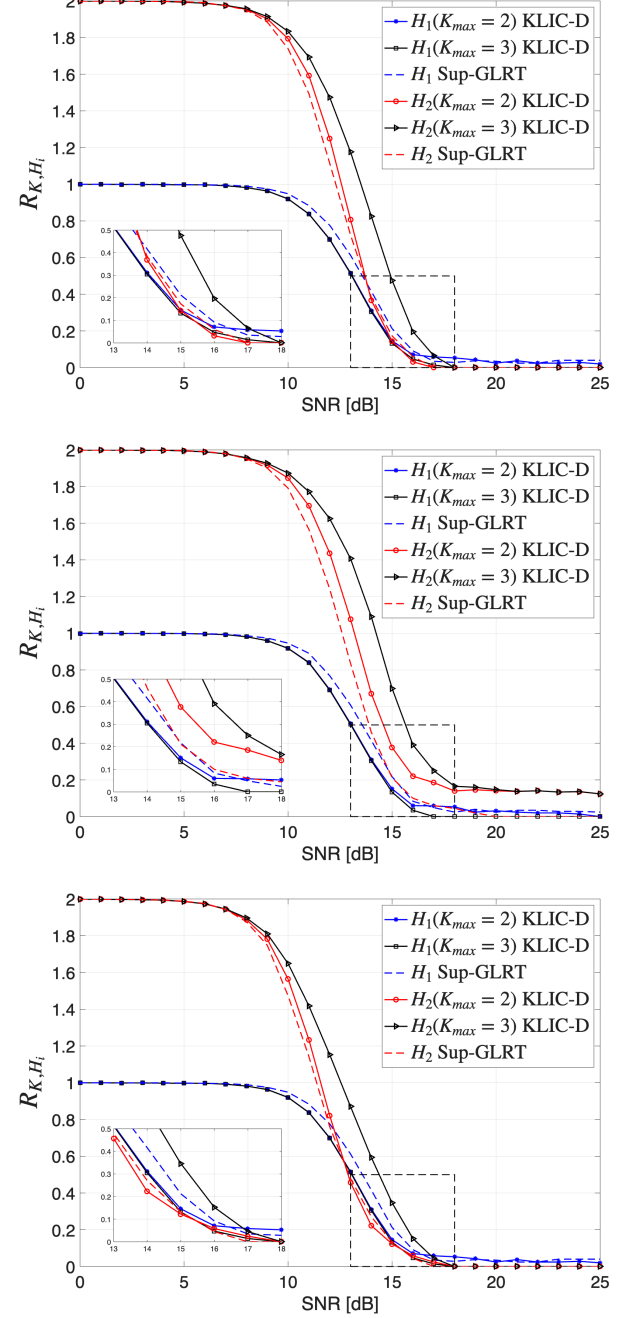


Fig. 7. Root Mean Square Error R_{K,H_i} , $i = 1, 2$ versus SNR [dB], assuming the same scattering coefficients and fixed positions (at the top) and random positions (at the middle), assuming different scattering coefficients and fixed positions (at the bottom).

of the compressive sensing paradigm within the KLIC-D framework does not compromise parameter estimation quality. For the fixed-position configurations, varying the scatterer powers did not significantly affect height RMSE, likely due to the dominance of the spatial separation in the estimation error.

Overall, these results validate the effectiveness of the proposed method in detecting multiple scatterers even under moderate SNR conditions. The results also demonstrate robustness against power imbalances while maintaining comparable detection performance with respect to Sup-GLRT. Moreover, while the Sup-GLRT is limited in practice to $K_{\max} = 2$ due to its sequential, multi-stage detection process, the proposed method can be set to manage more than two scatterers, while maintaining reliable performance in the presence of two scatterers. This is corroborated by the performance analysis, where in the presence of 2 PSs, the detector maintains a high probability of detection and correct classification as well as low RMSE values even with $K_{\max} = 3$. In some cases, for high SNR values, the RMSE returned by the proposed procedure could be slightly higher than that of the Sup-GLRT. This behavior might be due to the fact that for high SNR values the sidelobes of the sparse response associated with each scatterer might interfere with the respective mainlobes.

3) Performance analysis of KLIC-D in case of $K_{\max} = 3$: In the following, the random position scenario is considered to further investigate the behavior of the KLIC-D, when H_i , $i = 1, 2, 3$, are in force.

Figure 13 shows P_{d,H_i} , $i = 1, 2, 3$ as a function of the SNR assuming different backscattering, where, the scatterers' power levels are set as follows:

- under H_1 , $|g_1|^2 = g^2$;
- under H_2 , $|g_1|^2 = g^2$ and $|g_2|^2 = 1.5g^2$;
- under H_3 , $|g_1|^2 = g^2$, $|g_2|^2 = 1.5g^2$, and $|g_3|^2 = 2g^2$.

As the SNR increases, the probability of detection improves consistently. The detection probability curve for H_3 shifts to the left, indicating improved detection due to the contribution of the stronger scatterer. This behavior indicates that stronger scatterers enhance the overall detection performance, allowing the decision scheme to distinguish multiple scatterers even with medium values of SNR.

Figure 14 illustrates R_{K,H_i} , $i = 1, 2, 3$, as a function of the SNR. As expected, the estimation error decreases as the SNR increases, indicating that the detector provides more accurate estimates of the number of scatterers in the high SNR regime. Moreover, as the number of scatterers grows, the estimation quality decreases due to the increase of the number of unknown parameters.

Before concluding this section, we further consider an experiment in a realistic urban scenario by simulating the presence of a building with a height of approximately 89.2 m, and the surrounding floor level at $z = 0$. The simulation assumes the presence of single scatterers located on the floor at near ranges, followed by pixels characterized by the interference of three scatterers from floor, façade,

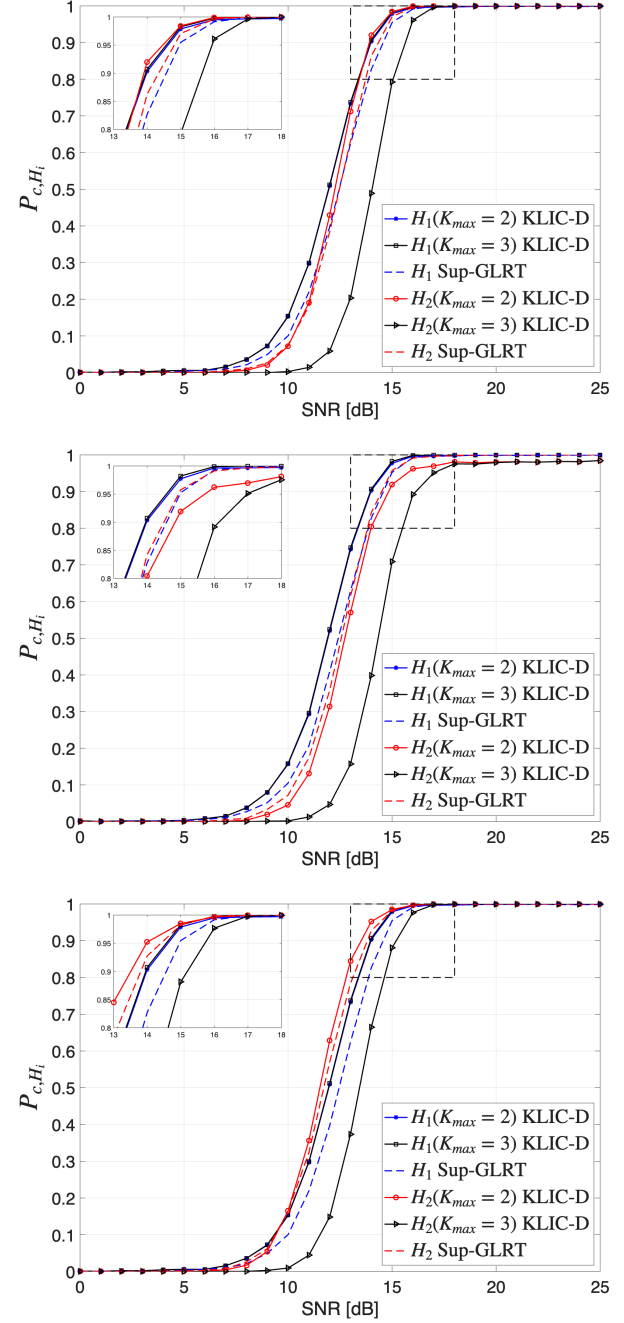


Fig. 8. Probability of correct classification P_{c,H_i} versus SNR [dB], assuming the same scattering coefficients with fixed positions (at the top), random positions (at the middle), and assuming different scattering coefficients with fixed positions (at the bottom).

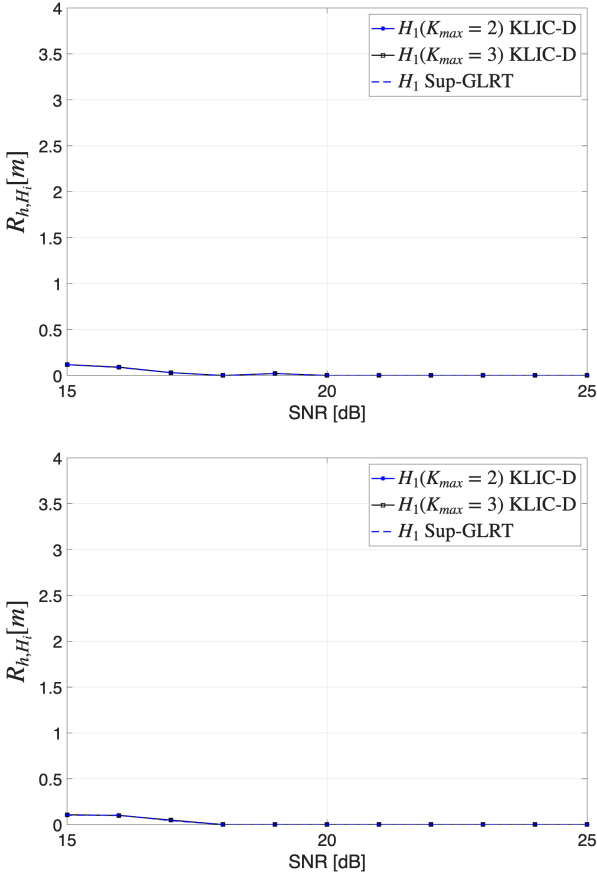


Fig. 9. RMSE for scatterer height estimation [m] versus SNR under H_1 , assuming fixed positions (at the top) and random positions (at the bottom).

and roof, and, finally, in far range pixels, interference from two scatterers on the floor and façade only. We set $\text{SNR}=15$ dB, $g_{\text{floor}}=g_{\text{roof}}=1$, and $g_{\text{façade}}=1.5$. Received data are simulated according to the previously mentioned system parameters and baseline distributions. The values are averaged over 100 iterations and KLIC-D uses $K_{\max}=3$. The results are shown in Figure 15. It is evident that the method allows us to achieve an accurate reconstruction, including a correct handling of the triple interferences.

A final remark on the computational load is now in order. As underlined at the end of Section III.A, the time of convergence of the compressive sensing algorithm is independent of K_{\max} . Moreover, experimentation on simulated data has shown that the algorithm converges in very few iterations, making the time required to estimate the scatterers parameters practically acceptable for each value of K_{\max} . On the other hand, Sup-GLRT estimates the scatterers parameters by scanning a multidimensional grid obtained by performing K_{\max} times the Cartesian product of the search grid used for a single scatterer with itself, making it practically unfeasible for $K_{\max} \geq 3$.

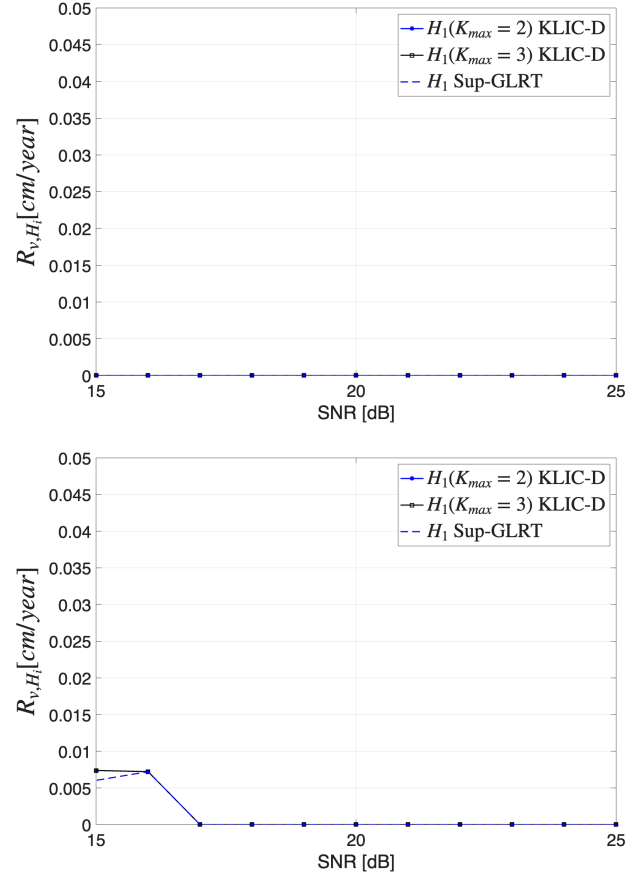


Fig. 10. RMSE of scatterer velocity estimation [cm/year] versus SNR under H_1 , assuming fixed positions (at the top) and random positions (at the bottom).

V. Experimental Results on Real data

To test the effectiveness of the proposed detection strategy in real scenarios, we apply the proposed detector on a real dataset relevant to an urbanized environment and consisting of 38 SAR images acquired by the COSMO-SkyMed constellation over the city of Naples, South Italy. Data have been acquired from January 2017 to September 2019, on ascending passes (HIMAGE mode) of the satellites. The acquisition system parameters as well as the distribution of the baselines are the same already exploited also for the simulations in the previous section, see Figure 3. The temporal average amplitude of the selected test site is provided in Figure 16, whereas the corresponding optical image from Google Earth is shown in Figure 17: this area contains the city central station, whose platforms and tracks are easily recognizable in the bottom part of the images, as well as the business district, in the central part, characterized by the presence of a cluster of skyscrapers, most of them about 100 m tall, which lead to a frequent occurrence of layover effects.

The dataset was preliminary phase-calibrated with respect to the contributions associated with the atmospheric phase screen and large-scale deformations through the

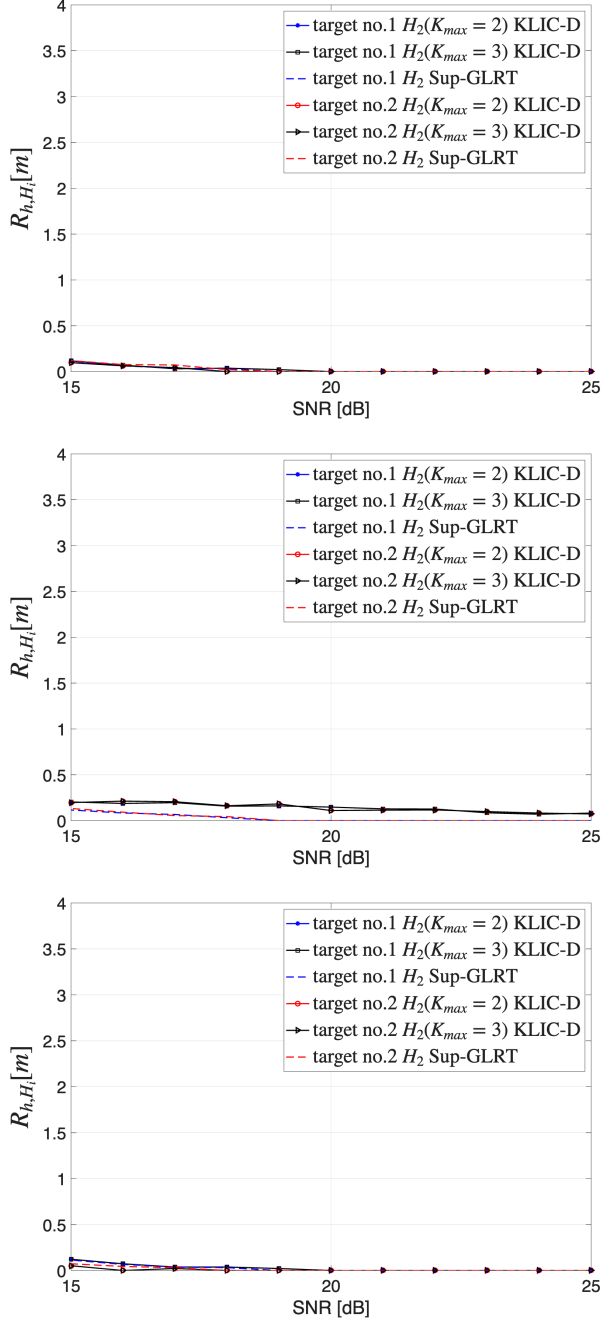


Fig. 11. RMSE for height estimation [m] versus SNR under H_2 , assuming the same scattering coefficients with fixed positions (at the top), random positions (at the middle), and different scattering coefficients with fixed positions (at the bottom).

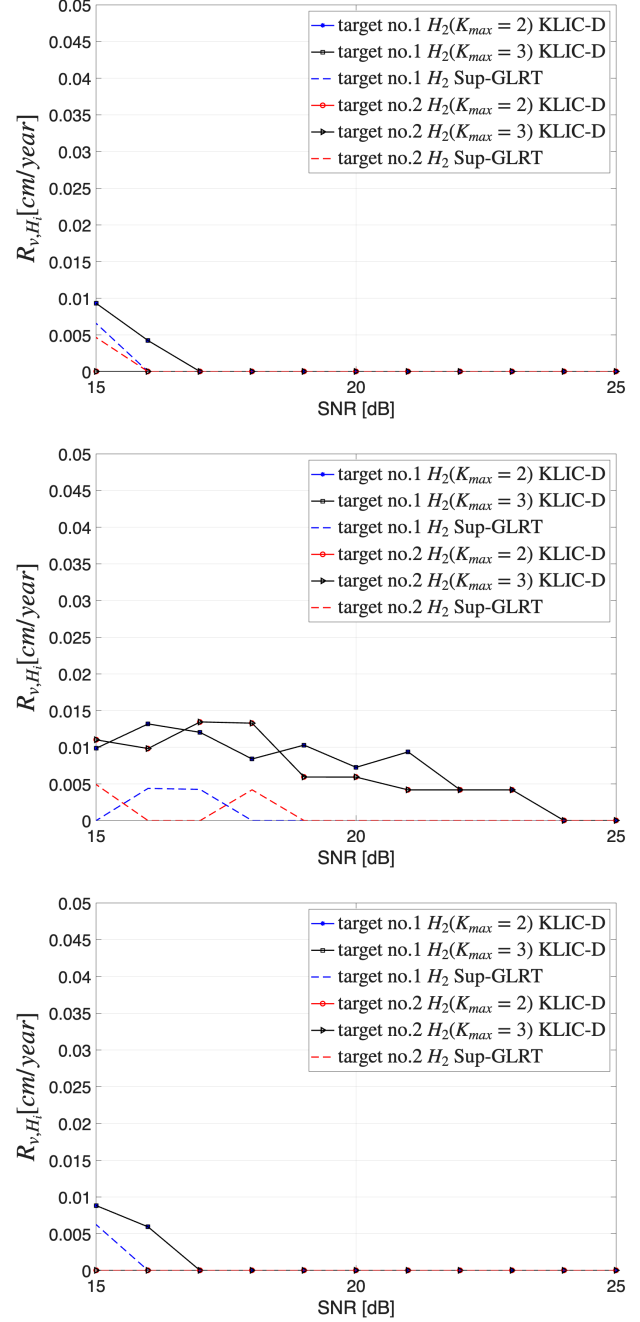


Fig. 12. RMSE for velocity estimation [cm/year] versus SNR under H_2 , assuming the same scattering coefficients with fixed positions (at the top), random positions (at the middle), and different scattering coefficients with fixed positions (at the bottom).

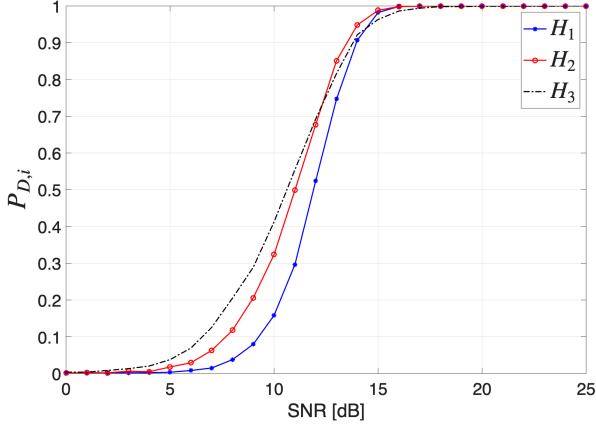


Fig. 13. KLIC-D P_{d,H_i} , $i = 1, 2, 3$ versus SNR [dB], assuming different scattering coefficients.

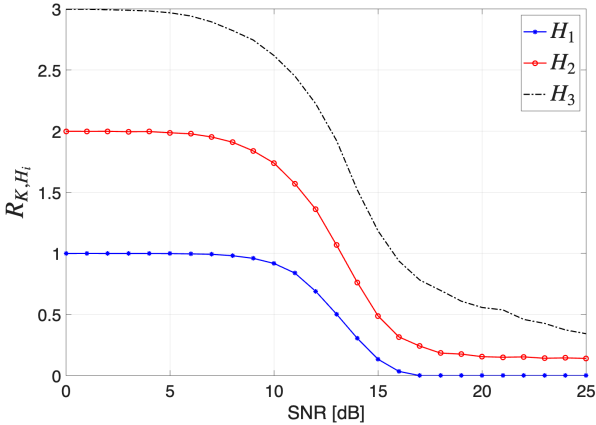


Fig. 14. KLIC-D R_{K,H_i} , $i = 1, 2, 3$ versus SNR [dB], assuming different scattering coefficients.

implementation of the procedure described in [32] which first exploit a Small-Baseline processing [5] at a lower spatial resolution. Data have been also referenced to an external Shuttle Radar Topography Mission (SRTM) Digital Elevation Model (DEM) [33].

Following the same line of reasoning as in the previous section, we firstly compare the performances of the KLIC-D with Sup-GLRT by limiting the maximum number of expected scatterers to $K_{\max} = 2$. The parameters of the processing, specifically, the search grids and thresholds are set according to the performance analysis in Section IV. The distribution of the detected single scatterers is provided in Figure 18, where the estimated residual topography z , with respect to the exploited DEM, and velocity v , with respect to the calibrated large-scale deformation, are represented. The results show a very good agreement of the two detectors both in terms of number of detected single scatterers and in terms of estimated parameters. The estimated residual topography shows typical height

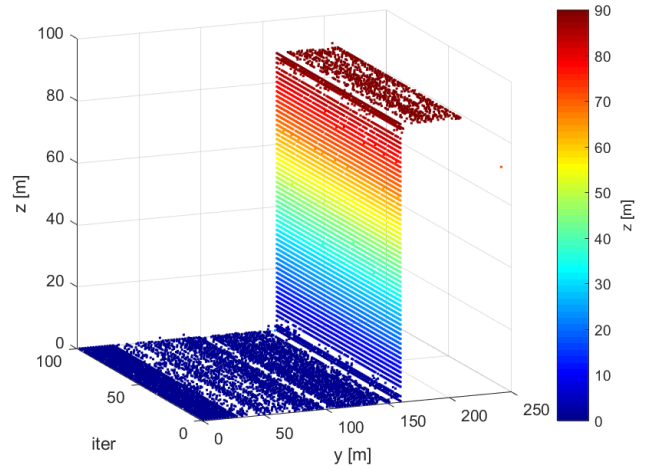
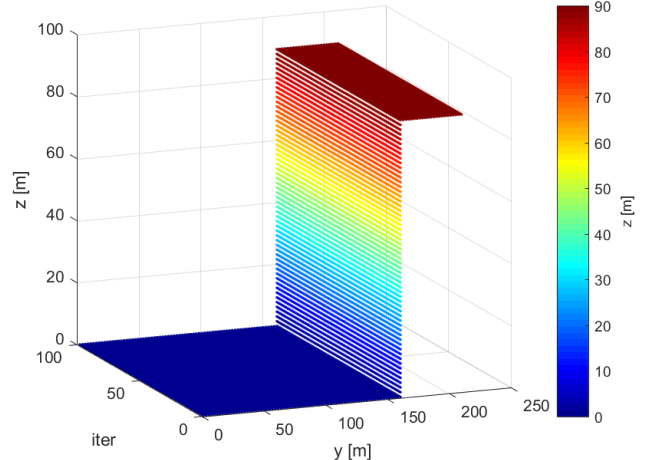


Fig. 15. 3D scatter plots of the simulated scenario: (top) simulated building and (bottom) reconstruction from scatterers detected by KLIC-D with $K_{\max} = 3$.

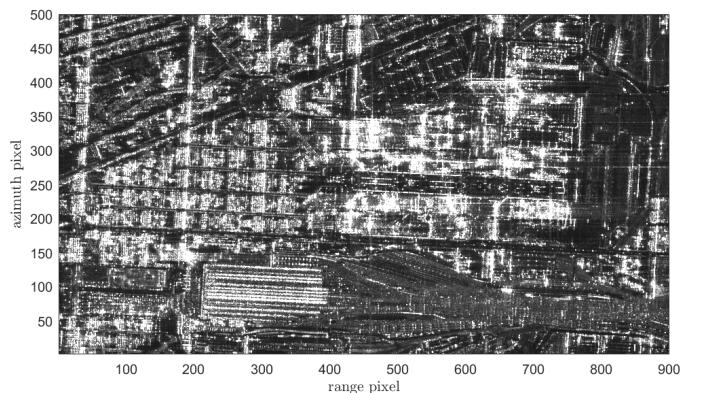


Fig. 16. Temporal average amplitude image of the COSMO-SkyMed dataset over the city of Naples, South Italy. Horizontal and vertical directions corresponds to range and azimuth, respectively.



Fig. 17. Tilted view from Google Earth corresponding (white frame) to the radar image in Figure 16. In light-blue the area corresponding to the zoom of the results in subsequent Figure 22.

ramps in correspondence of skyscraper footprints whereas (residual) velocities do not show any significant localized deformation. The histograms of the differences of the estimated parameters over the mask of overlapping detected pixels, normalized to the sampling step, set as half of the theoretical Rayleigh resolutions for both elevation and velocity, show that the two methods estimate the same height over more than the 94.4% and the same velocity over the 97.8% of the common detected pixels. In any case, the residual difference is mainly confined to ± 1 sample. In terms of detection, the proposed method detects 1.8% more single scatterers than Sup-GLRT, see Table I.

The distribution of the detected double scatterers is provided in Figure 20, where the residual topography associated to the higher and lower layers of detected scatterers is represented. It is well evident the different pattern for both detection schemes, between the higher level, showing more height variations being likely associated to scatterers located on buildings, and the lower level, showing a more uniform pattern as associated to scatterers lying on the ground. The velocity, being consistent with that of single scatterers and not showing significant different patterns between the detected double scatterers is not shown for brevity. In terms of detection performances, the KLIC-D shows a reduction in the number of detected double scatterers quantified in about 30% than those detected by Sup-GLRT, see Table I. In general, by counting the number of pixels for which at least one scatterer has been detected, compliant with the definition of P_d in Section IV, the two schemes performs almost the same, with a slight difference of 3.1% in favor of Sup-GLRT. This is compatible with the detection performances provided in Figure 6, where the two detectors shows comparable P_{dS} , slightly in favor of Sup-GLRT. Based on outcomes of RMSE in Figure 7, the detection loss of KLIC-D on double scatterers could be induced by the slower decreasing of the error with respect to SNR.

The strength of the proposed method stands, however, in the possibility to increase the order of the maximum possible detectable scatterers without increasing the computational cost, differently from Sup-GLRT which cannot be extended so effortlessly. The results of the implementation of the proposed detector for $K_{\max} = 3$ are provided

TABLE I
Number of detected scatterers - $K_{\max} = 2$

	Sup-GLRT	KLIC-D	% variation
single scatterers	136126	138562	+1.8%
double scatterers	24631	17249	-30%
Total	160757	155811	-3.1%

TABLE II
Number of detected scatterers - $K_{\max} = 3$

# of PS	KLIC-D
1	138266
2	16722
3	959
Total	155947

in Figure 21, where the estimated residual topography and velocity for single and higher layer of double and triple scatterers are represented. The results of both single and double scatterers are in accordance with those of Figures 18 and 20. Additionally, the estimation of the sparse triple scatterers do not show significant anomalies compared to the former two. In terms of number of detected scatterers, it results from Table II that the number of total scatterers, for which at least one scatterer is detected, is almost the same as for the case of $K_{\max} = 2$. This is reasonable with the working principle of the proposed detector that, by increasing K_{\max} , extends the test to the increased number of potential peaks provided by the CS estimation.

The 3-D point cloud of scatterers detected by KLIC-D with $K_{\max} = 3$ in the area delimited by the light-blue frame in Figure 17, after geocoding from the native radar (azimuth; range) geometry to a geographical (East; North; Height) reference system is provided in Figure 22. The shapes of the dense building texture can be easily recognized as well as the more uniform pattern corresponding to the station and platforms in the bottom-right part of the image. False alarms are detected in correspondence of very strong backscattering sources leading to significantly large focusing sidelobes, see also Figure 16, although Hamming filtering was applied in the focusing process. Mitigation of those sidelobes [34], that would be beneficial, is however out of the scope of this work.

VI. Conclusion

In this work we have introduced a novel decision scheme in the framework of SAR Tomography to detect interfering scatterers within the same same resolution cell. The detector relies on an information-theoretic design framework and allows us to solve multiple hypothesis test formed by one null hypothesis and multiple alternative hypotheses. For the specific case, each alternative hypothesis correspond to a given number of scatterers. Remarkably, this approach leads to the same decision scheme as that proposed in [14] when only one PS is

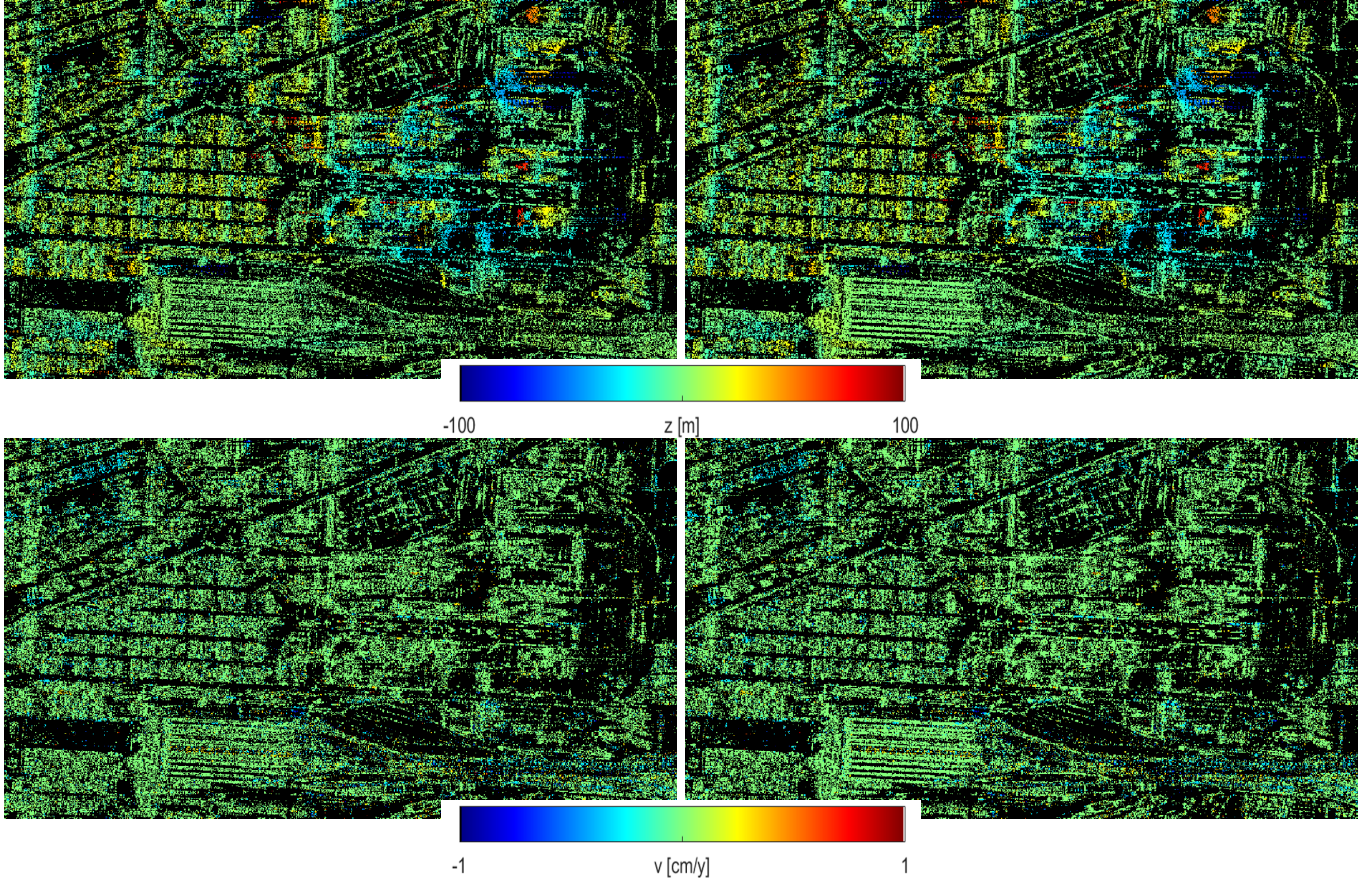


Fig. 18. Spatial distribution of detected single scatterers by (left column) Sup-GLRT and (right column) KLIC-D, in case of $K_{\max} = 2$. (First row) estimated residual topography, (second row) estimated velocity. Colormap is set according to the values of the estimated parameters.

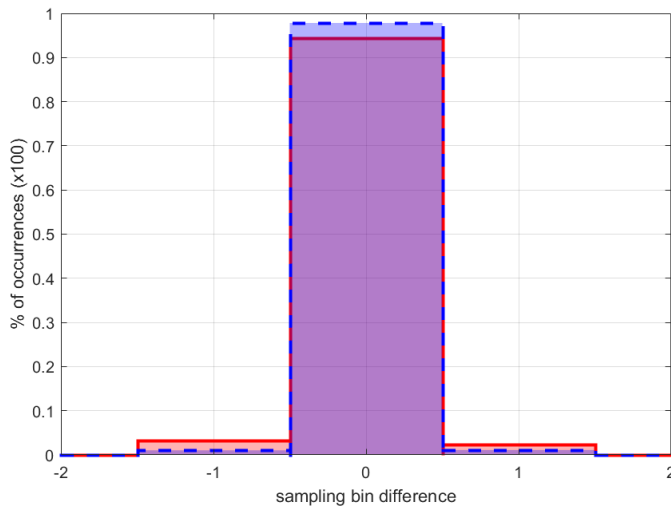


Fig. 19. Histogram of estimation differences provided by the Sup-GLRT and the KLIC-D for (red, solid line) height and (blue, dashed line) velocity. Horizontal axis is normalized to the corresponding sampling step.

present. In order to limit the computational burden, we have coupled the KLIC-based design framework proposed in [3] with the compressive sensing. Doing so, the resulting new detector exhibits a significant practical value since it does not require a number of classification/detection threshold that grows with the number of PSs unlike existing multistage approaches. At the same time, the performance assessment, carried out on both synthetic and real data, has shown that the detection/classification results are similar to that of the Sup-GLRT [2] that is the most natural competitor due to its scalability according to the number of PSs.

Future research tracks might encompass the assessment of a detector obtained by further iterating the estimation of the unknown parameters as well as the design under more involved interference models. Another interesting research track concerns the design of two stage architectures formed by cascading the proposed estimation algorithm (or other grid-based efficient solutions) and a gridless estimation method that exploits the rough estimates provided by the first stage as initial points.

Acknowledgment

The Authors would like to thank the Italian Space Agency (ASI) for providing the COSMO-SkyMed dataset.

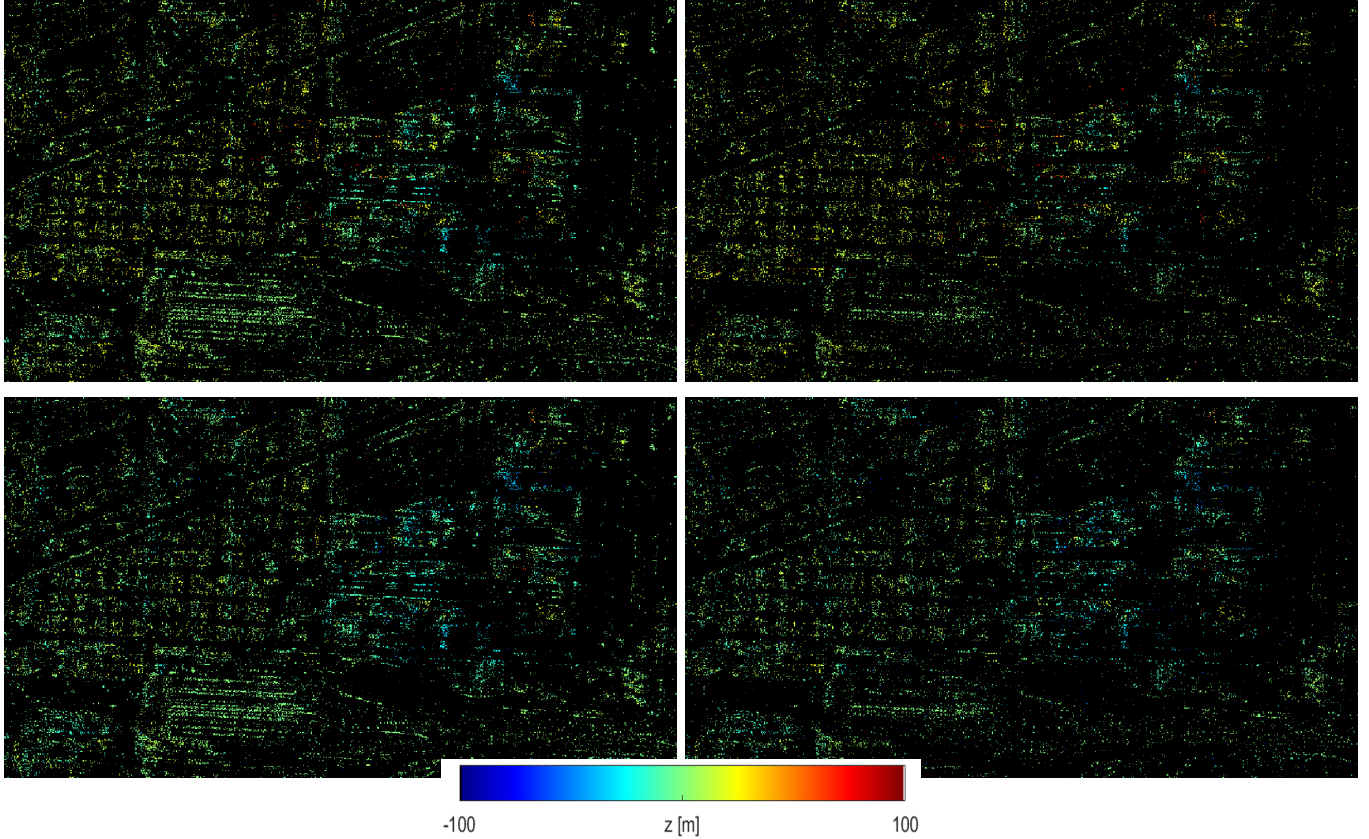


Fig. 20. Spatial distribution of detected double scatterers by (left column) Sup-GLRT and (right column) KLIC-D, in case of $K_{\max} = 2$. (First row) higher and (second row) lower layer of estimated residual topography. Colormap is set according to the values of the estimated parameters.

References

- [1] A. Pauciullo, D. Reale, A. De Maio, and G. Fornaro, "Detection of Double Scatterers in SAR Tomography," *IEEE Trans. Geosci. Remote Sens.*, vol. 50, no. 9, pp. 3567–3586, Sep. 2012.
- [2] A. Budillon and G. Schirinzi, "Glrt based on support estimation for multiple scatterers detection in sar tomography," *IEEE Journal of Selected Topics in Applied Earth Observations and Remote Sensing*, vol. 9, no. 3, pp. 1086–1094, 2015.
- [3] P. Addabbo, S. Han, F. Biondi, G. Giunta, and D. Orlando, "Adaptive radar detection in the presence of multiple alternative hypotheses using Kullback-Leibler information criterion-part I: Detector designs," *IEEE Transactions on Signal Processing*, vol. 69, pp. 3730–3741, 2021.
- [4] A. Ferretti, C. Prati, and F. Rocca, "Permanent scatterers in sar interferometry," *IEEE Transactions on geoscience and remote sensing*, vol. 39, no. 1, pp. 8–20, 2001.
- [5] P. Berardino, G. Fornaro, R. Lanari, and E. Sansosti, "A new algorithm for surface deformation monitoring based on small baseline differential sar interferograms," *IEEE Transactions on geoscience and remote sensing*, vol. 40, no. 11, pp. 2375–2383, 2002.
- [6] A. Ferretti, C. Prati, and F. Rocca, "Nonlinear subsidence rate estimation using permanent scatterers in differential sar interferometry," *IEEE Transactions on geoscience and remote sensing*, vol. 38, no. 5, pp. 2202–2212, 2000.
- [7] A. Reigber and A. Moreira, "First demonstration of airborne sar tomography using multibaseline l-band data," *IEEE Transactions on Geoscience and Remote Sensing*, vol. 38, no. 5, pp. 2142–2152, 2000.
- [8] G. Fornaro, F. Serafino, and F. Soldovieri, "Three-dimensional focusing with multipass SAR data," *IEEE Trans. Geosci. Remote Sens.*, vol. 41, no. 3, pp. 507–517, March 2003.
- [9] G. Fornaro, F. Lombardini, and F. Serafino, "Three-Dimensional Multipass SAR Focusing: Experiments With Long-
- [10] G. Fornaro, D. Reale, and F. Serafino, "Four-Dimensional SAR Imaging for Height Estimation and Monitoring of Single and Double Scatterers," *IEEE Trans. Geosci. Remote Sens.*, vol. 47, no. 1, pp. 224–237, Jan. 2009.
- [11] X. X. Zhu and R. Bamler, "Very High Resolution Spaceborne SAR Tomography in Urban Environment," *IEEE Trans. Geosci. Remote Sens.*, vol. 48, no. 12, pp. 4296–4308, Dec. 2010.
- [12] D. Reale, G. Fornaro, and A. Pauciullo, "Extension of 4-d sar imaging to the monitoring of thermally dilating scatterers," *IEEE transactions on geoscience and remote sensing*, vol. 51, no. 12, pp. 5296–5306, 2013.
- [13] X. X. Zhu and R. Bamler, "Let's Do the Time Warp: Multi-component Nonlinear Motion Estimation in Differential SAR Tomography," *IEEE Geosci. Remote Sens. Lett.*, vol. 8, no. 4, pp. 735–739, Jul. 2011.
- [14] A. De Maio, G. Fornaro, and A. Pauciullo, "Detection of Single Scatterers in Multidimensional SAR Imaging," *IEEE Trans. Geosci. Remote Sens.*, vol. 47, no. 7, pp. 2284–2297, Jul. 2009.
- [15] A. Budillon, A. C. Johns, and G. Schirinzi, "A fast support detector for superresolution localization of multiple scatterers in sar tomography," *IEEE Journal of Selected Topics in Applied Earth Observations and Remote Sensing*, vol. 10, no. 6, pp. 2768–2779, 2017.
- [16] E. J. Candès, J. Romberg, and T. Tao, "Robust uncertainty principles: Exact signal reconstruction from highly incomplete frequency information," *IEEE Transactions on information theory*, vol. 52, no. 2, pp. 489–509, 2006.
- [17] X. X. Zhu and R. Bamler, "Tomographic sar inversion by l_1 -norm regularization—the compressive sensing approach," *IEEE transactions on Geoscience and Remote Sensing*, vol. 48, no. 10, pp. 3839–3846, 2010.
- [18] A. Budillon, A. Evangelista, and G. Schirinzi, "Sar tomography

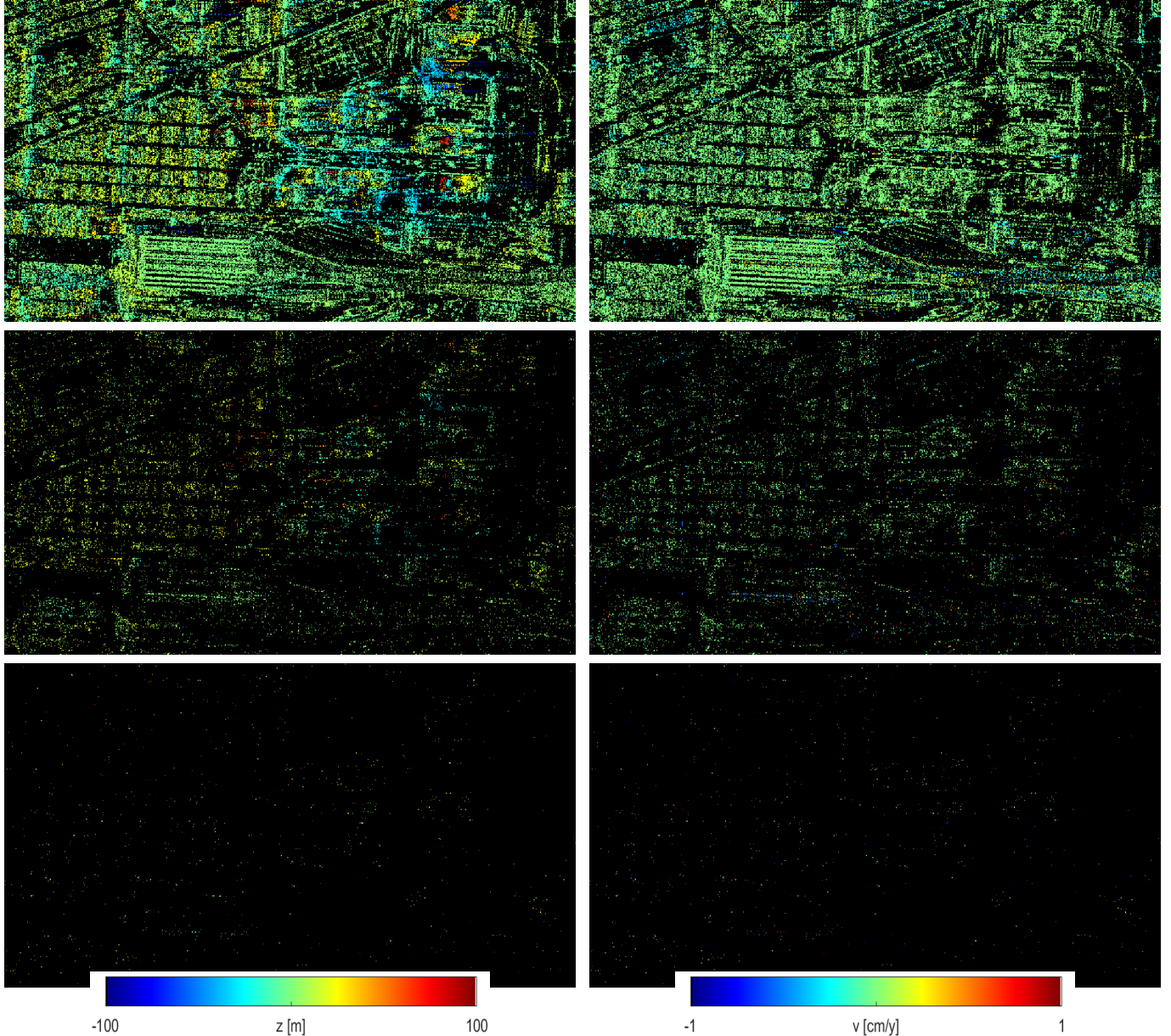


Fig. 21. Spatial distribution of triple scatterers detected by KLIC-D for $K_{\max} = 3$. Estimated (left column) residual topography and (right) velocity for (first row) # of PS = 1, (second row) # of PS = 2 and (third row) # of PS = 3. Colormap is set according to the values of the estimated parameters.

from sparse samples,” in *2009 IEEE international geoscience and remote sensing symposium*, vol. 4. IEEE, 2009, pp. IV–865.

[19] ——, “Three-dimensional sar focusing from multipass signals using compressive sampling,” *IEEE Transactions on Geoscience and Remote Sensing*, vol. 49, no. 1, pp. 488–499, 2010.

[20] X. X. Zhu and R. Bamler, “Super-resolution power and robustness of compressive sensing for spectral estimation with application to spaceborne tomographic sar,” *IEEE Transactions on Geoscience and Remote Sensing*, vol. 50, no. 1, pp. 247–258, 2011.

[21] N. Haddad, K. Hadj-Rabah, A. Budillon, and G. Schirinzi, “Beyond the grid: Glrt-based tomosar fast detection for retrieving height and thermal dilation,” *Remote Sensing*, vol. 17, no. 14, 2025. [Online]. Available: <https://www.mdpi.com/2072-4292/17/14/2334>

[22] G. D. Martín-del Campo-Becerra, S. A. Serafín-García, A. Reigber, and S. Ortega-Cisneros, “Parameter selection criteria for tomo-sar focusing,” *IEEE Journal of Selected Topics in Applied Earth Observations and Remote Sensing*, vol. 14, pp. 1580–1602,

2021.

[23] P. Stoica and Y. Selen, “Model-order selection: A review of information criterion rules,” *IEEE Signal Processing Magazine*, vol. 21, no. 4, pp. 36–47, 2004.

[24] N. Haddad, A. Budillon, K. Hadj-Rabah, A. Bouaraba, L. Harkati, M. A. Benbouzid, and G. Schirinzi, “Gridless glrt for tomographic sar detection using particle swarm optimization algorithm,” *IEEE Geoscience and Remote Sensing Letters*, vol. 21, pp. 1–5, 2024.

[25] S. Kullback and R. A. Leibler, “On information and sufficiency,” *The annals of mathematical statistics*, vol. 22, no. 1, pp. 79–86, 1951.

[26] A. Pauciullo, D. Reale, W. Franzé, and G. Fornaro, “Multi-look in glrt-based detection of single and double persistent scatterers,” *IEEE Transactions on Geoscience and Remote Sensing*, vol. 56, no. 9, pp. 5125–5137, 2018.

[27] P. Addabbo, S. Han, F. Biondi, G. Giunta, and D. Orlando, “Adaptive Radar Detection in the Presence of Multiple Alternative Hypotheses Using Kullback-Leibler Information Criterion-

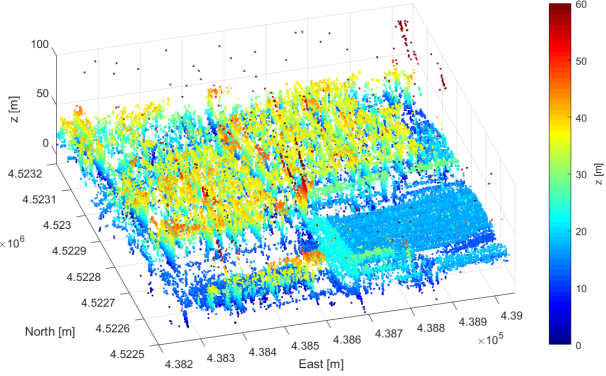


Fig. 22. 3-D point cloud of scatterers detected by KLIC-D ($K_{\max} = 3$) on the area delimited by the light-blue frame in Figure 17.

Part II: Applications," *IEEE Transactions on Signal Processing*, vol. 69, pp. 3742–3754, 2021.

[28] P. Stoica, Y. Selen, and J. Li, "On information criteria and the generalized likelihood ratio test of model order selection," *IEEE Signal Processing Letters*, vol. 11, no. 10, pp. 794–797, 2004.

[29] K. Murphy, *Machine Learning: A Probabilistic Perspective*, ser. Adaptive Computation and Machine Learning series. MIT Press, 2012.

[30] S. Han, Y. Zhang, C. Hao, J. Liu, A. Farina, and D. Orlando, "Sparsity-Based Classification Approaches for Radar Data in the Presence of Clutter Edges and Discretes," *IEEE Transactions on Aerospace and Electronic Systems*, vol. 59, no. 3, pp. 2141–2162, 2023.

[31] H. Lütkepohl, *Handbook of Matrices*. Wiley, 1997.

[32] G. Fornaro, F. Lombardini, A. Pauciullo, D. Reale, and F. Viviani, "Tomographic processing of interferometric sar data: Developments, applications, and future research perspectives," *IEEE Signal Processing Magazine*, vol. 31, no. 4, pp. 41–50, 2014.

[33] T. G. Farr, P. A. Rosen, E. Caro, R. Crippen, R. Duren, S. Hensley, M. Kobrick, M. Paller, E. Rodriguez, L. Roth, D. Seal, S. Shaffer, J. Shimada, J. Umland, M. Werner, M. Oskin, D. Burbank, and D. Alsdorf, "The Shuttle Radar Topography Mission," *Reviews of Geophysics*, vol. 45, no. 2, 2007.

[34] R. Iglesias and J. J. Mallorqui, "Side-Lobe Cancelation in DInSAR Pixel Selection With SVA," *IEEE Geoscience and Remote Sensing Letters*, vol. 10, no. 4, pp. 667–671, 2013.